A study of the magnetic properties and the magneto-crystalline anisotropy for the nano-composites CoFe$_2$O$_4$/Sm$_{0.7}$La$_{0.3}$FeO$_3$

Ebtesam E. Ateia[1] , M. K. Abdelmaksoud[1,2], and H. Ismail[1,*]

[1] *Faculty of Science, Physics Department, Cairo University, Giza 12613, Egypt*
[2] *Faculty of Nanotechnology for Postgraduate Studies, Cairo University, El-Sheikh Zayed 12588, Egypt*

ABSTRACT

In this study, nano-composites are formed as a mixture of spinel and a perovskite with various percentages to enhance their physical properties and applicability. The composites have the general form $(1\text{-}x)$ CoFe$_2$O$_4$ + x Sm$_{0.7}$La$_{0.3}$FeO$_3$; $0.0 \leq x \leq 1$. All the samples including the parents are thoroughly characterized to make sure of their crystallinity, single or double phase formation, and the percentages of the mixed components. Moreover, the crystallite size of the prepared samples, the infrared excitation of their functional groups, and their particle distribution are also comprehensively explored. The inspected samples display the spinel ferrites signature peaks at around 405 and 568 cm^{-1} with corresponding bond force constants of about 1×10^5 and 2×10^5 dyne/cm, respectively. The magnetic properties of samples at room temperature are discussed with extensive elaboration on the critical size and the magneto-crystalline anisotropy constant. The Stoner–Wohlfarth model has been applied to find the cubic anisotropy constant of CoFe$_2$O$_4$ which agrees pretty well with prior published data.

1 Introduction

The spinel AB$_2$X$_4$ is one of the most remarkable crystalline compounds, with a vast range of applications. In the normal spinel structure, A, B, and X represent a divalent cation, a trivalent cation, and a divalent anion, respectively. Spinel ferrites and, in particular, the cobalt ferrites have been studied extensively due to their outstanding performance in high-frequency devices and many other appliances [1]. Moreover, Cobalt ferrite is a hard magnetic material whose magnetic properties exhibit size dependence. It displays many intriguing properties, like high coercivity, excellent chemical stability, good mechanical hardness, and strong anisotropy [2]. CoFe$_2$O$_4$ (CFO) is forming in a cubic inverse-spinel structure and belongs to the square group O_h^7 (Fd3m) [3].

On the other hand, Perovskites are complex oxides with a common ABO$_3$ crystal structure. Specifically,

Address correspondence to E-mail: heba.torky25@yahoo.com

rare earth (RE) ortho-ferrites, $REFeO_3$, have a tilted orthorhombic perovskite structure. The physical properties of a perovskite may change considerably by the slight elemental substitution in the cation sites. Lanthanum and samarium ferrites display the orthorhombic perovskite structure with space group Pbnm. In the ideal perovskite structure, the A- and B-site cations are coordinated with six and 12 oxygen anions, respectively [4].

Furthermore, cobalt, lanthanum, and samarium ferrites have gained a growing attention as a result of their enormous applications, for instance, magnetic recording and storage [5], magnetic stress sensor [6], solid oxide fuel cells [7], gas sensors [8], photo-catalytic degradation [9], and biomedical [10] as well as antibacterial and anti-biofilm activities [11].

Moreover, rare earth- (A-site-doped) ortho-ferrite with the general formula, $La_{1-x}RE_xFeO_3$, and similar compounds are considered as promising materials due to their potential utilization in numerous technological, environmental, and medical fields [4].

The aim of the present work is to optimize the physical properties of the spinel/perovskite nano-composites. Explicitly, the nano-composites $(1-x)$ $CoFe_2O_4 + x\ Sm_{0.7}La_{0.3}FeO_3$; $x = 0, 0.3, 0.5, 0.7,$ and 1 are characterized and their structural and magnetic properties are thoroughly investigated so as to find the optimum nano-composite of the inspected samples. The chosen specific percentages of the doped perovskite are elected from a prior study, submitted for publication, as the optimum of a series of doped samples.

2 Experimental

$Sm_{0.7}La_{0.3}FeO_3$ (SLFO) and $CoFe_2O_4$ (CFO) powder were synthesized by citrate–nitrate auto combustion method using samarium nitrate ($Sm(NO_3)_3.6H_2O$), lanthanum Nitrate ($La(NO_3)_3.6H_2O$), ferric nitrate ($Fe(NO_3)_3 \cdot 9H_2O$), cobalt nitrate($Co(NO_3)_2.6H_2O$), and citric acid ($C_6H_8O_7 \cdot H_2O$) as starting materials as shown in Fig. 1 The raw materials were weighted according to stoichiometric ratio and dissolved in minimum amount of distilled water. Citric acid has been added in the molar ratio (1:1 to metal nitrates). The pH of the solution was adjusted to 7 by dropwise addition of ammonia with constant magnetic stirring. The solution was heated on a hot plate until excess free water evaporated. This was followed by

ignition. Within a few seconds, the combustion reaction completed. The collected powder was grinded for 2 h using a gate mortar and then heated at 600 °C for 1 h by rate 4 °C/min then grinding the powder for 2 h.

SLFO powder was mixed thoroughly with CFO and grinded for 2 h at room temperature with different ratios (30:70, 50:50 and 70:30). The nano-composite samples were sintered at 200 °C for 2 h by rate 4 °C/min. X–ray studies were carried out by X-ray diffractometer using X-ray diffraction (XRD), Philips Pu 1390 channel control using Cu-K_α target. The morphology and grain size distribution are inspected using the high-resolution transmission electron microscope (HRTEM), type JEOL-JEM 2100. Field emission scanning electron microscope (FESEM, type Philips- QUANTA FEG 250) was applied to visualize microscopic topographical details on the surface. The chemical composition of the composites was checked by energy-dispersive X-ray analysis which is attached to the FESEM. Before imaging, the samples were coated with Au. FTIR spectra were recorded on a Nicolet 380 FTIR Spectrometer. Finally, the magnetic properties were analyzed at room temperature using a vibrating sample magnetometer (VSM, Lake Shore Model 7410, USA).

3 Results and discussion

3.1 Structural analysis

The X-ray diffraction (XRD) patterns of the $(1-x)$ (CFO) + x (SLFO); $x = 0, 0.3, 0.5, 0.7,$ and 1 composites are shown in Fig. 2. Data were collected in the 2θ range from 10 to 80°. XRD pattern for CFO/SLFO nano-composite shows there is no detected foreign phases in addition to those concerning CFO and SLFO. This indicates that the two composite phases exist separately, without any chemical interaction, and display outstanding chemical compatibility. However, slight changes in the position of the peaks are observed indicating slim variation in the lattice constants of the corresponding phases.

The slight changes in the position of the peaks can be attributed to stress and/or structural defects created by the substitution of cobalt by rare earth ions. This confirms the continual structural distortion in the prepared composites with different

Fig. 1 Simple chart for the preparation technique
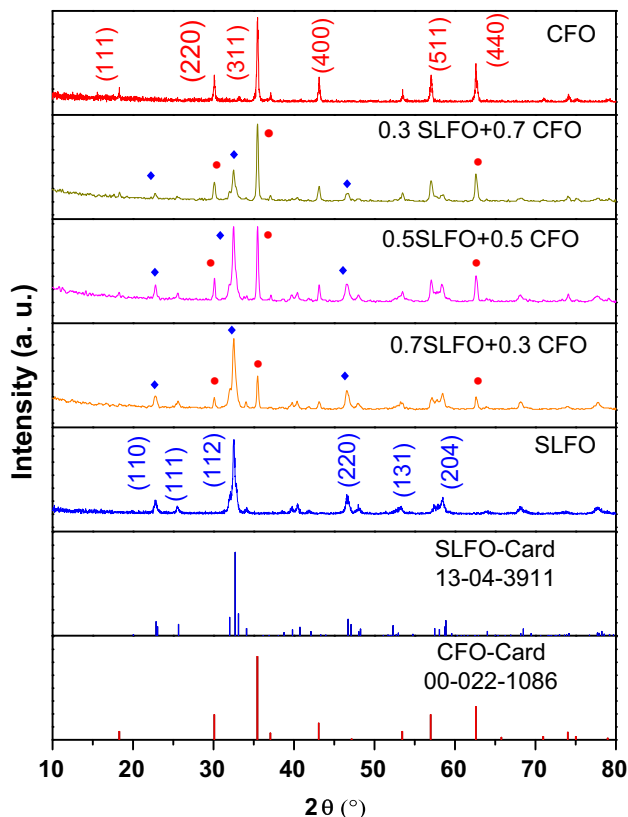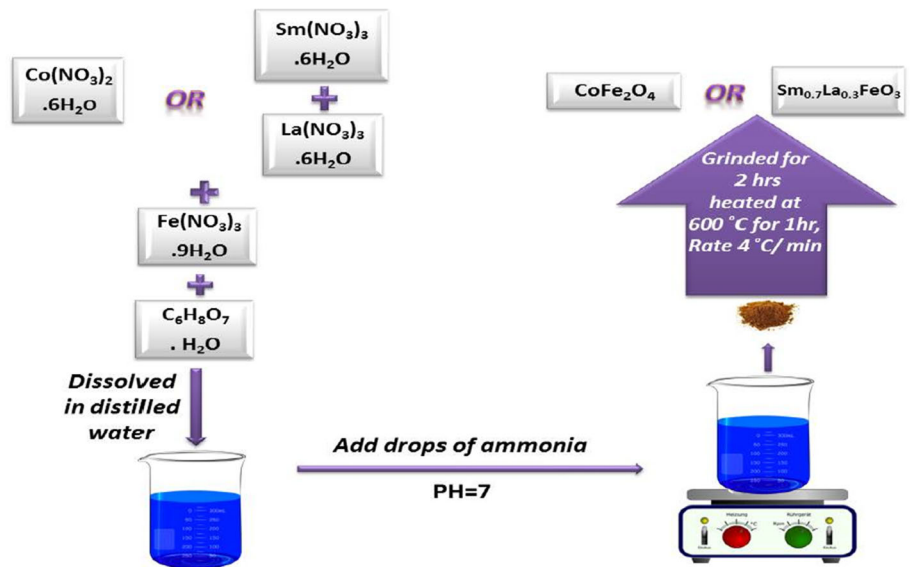
Fig. 2 X-ray diffraction of (1-x) CFO + x SLFO; x = 0, 0.3, 0.5, 0.7, and 1 samples

concentrations of the antiferromagnetic and hard magnetic phase.

The lattice constants (a, b and c) and unit cell volume (V) are calculated from the XRD data and recorded in Table 1. The unit cell volume of SLFO

component in the nano-composite is generally larger than its corresponding parent value and it is even increasing as the CFO percentage increases. For the CFO component, the lattice constants and unit cell volume rise relative to their corresponding parent value, except for x = 0.5. The theoretical density D_x was calculated from the straight forward formula

$$D_x = \frac{ZM}{N_A V_M} \tag{1}$$

where M is the molecular weight, Z is the number of molecules per unit cell, N_A is Avogadro's number, and V_M is the volume of a molecule. Table 1 shows that the density of SLFO in the nano-composite increases as its percentage, in the composite, increases. Moreover, the SLFO component density is less than that of the parent for all x-values. The average crystallite size (D_c) of the prepared nano-particles (NPs) was calculated using Debye–Scherrer equation [12]:

$$D_c = \frac{k\lambda}{\beta \cos\Theta} \tag{2}$$

with k is the shape factor, which usually takes a value of 0.89, λ is the Cu-k$_\alpha$ wavelength, β is the full width at half maximum in radians, and Θ is the diffraction angle. Explicitly, the average crystal size of SLFO phase expanded and that of CFO phase contracted as detected in Table 1.

Figure 3 shows the morphology of the prepared nano-composites using HRTEM with the selected area electron diffraction patterns (SAED) and "d"

Table 1 Average particle size, average crystal size (D_c), lattice constant, unite cell volume (V), and theoretical density (D_x) for (1-x) CFO + x SLFO; x = 0, 0.3, 0.5, 0.7, and 1 samples

| sample	Average particle size from (HRTEM) (nm)	Average crystallite size (D_c) (nm)	Lattice constants			Unit cell volume (V) Å^3	Theoretical density (D_x) g/cm^3
			a (Å)	b (Å)	c (Å)		
$CoFe_2O_4$	24	39.477	8.394	–	–	591.435	5.270
0.7 CFO + 0.3 SLFO							
$CoFe_2O_4$	21.6	26.766	8.396	8.396	8.396	591.805	5.266
$Sm_{0.7}La_{0.3}FeO_3$		19.111	5.502	5.590	7.774	239.105	6.966
0.5 CFO + 0.5 SLFO							
$CoFe_2O_4$	26.7	34.654	8.393	8.393	8.393	591.226	5.272
$Sm_{0.7}La_{0.3}FeO_3$		21.727	5.474	5.606	7.738	237.466	7.014
0.3 CFO + 0.7 SLFO							
$CoFe_2O_4$	36.6	34.256	8.396	8.396	8.396	591.896	5.266
$Sm_{0.7}La_{0.3}FeO_3$		17.033	5.454	5.589	7.740	235.928	7.059
$Sm_{0.7}La_{0.3}FeO_3$	–	15.08	5.439	5.602	7.737	235.77	7.065

spacing. The SAED diffraction patterns show spotted clustered rings which reflect the strong nano-crystallinity of the samples, in conformity with XRD data findings. All figures show agglomeration especially the $CoFe_2O_4$ sample. Comparing the nano-composites micrographs, it is clear that the "0.5CFO + 0.5 SLFO" sample shows the least agglomeration. The different micrographs display a non-uniform grain distribution of variable shape with well-defined boundaries with average grain size in the range of ∼ 21–35 nm. The HRTEM particle and XRD crystallite size values are inconsistent since NPs tend to accumulate to attain a lower free energy state. The observed accumulation is expected due to the interparticle interactions and the strong dipole–dipole magnetic interaction. This may explain the discrepancies between XRD crystallite and HRTEM particle sizes [13].

The various nano-composites HRTEM micrographs show a combination of cubic and orthorhombic particles which indicates that the composites contain the two phases in accordance with the physical mixing process.

The microstructure of the nano-composite samples, x = 0.3, 0.5, and 0.7, was analyzed using field emission scanning electron microscopy (FESEM) and the micrographs are presented in Fig. 4a–c. The samples were prepared onto a tape of carbon and coated with gold. The FESEM micrograph for (0.7 CFO + 0.3 SLFO) sample illustrates intercalated grains with coral-like morphology and it also shows the relatively

most porous nano-composite among the three samples. The micrographs for the other two nano-composites display a rocky-like aggregate with variable constellation sizes.

EDAX spectra deliberately investigate the detailed chemical composition of the synthesized nano-composites. The elemental analysis obtained from EDAX and the theoretical estimation of the atomic (At %) and weight (Wt %) percentages of individual elements (Sm, La, Co, Fe, and O) based on the chemical composition of the samples are shown as insets in Fig. 4d–f. The spectra emphasize the existence of the constituent elements of samarium, lanthanum, iron, cobalt, and oxygen. The nonappearance of impurities confirms the single-phase formation of the samples as appealed by XRD spectra. However, just a single peak of gold appears in Fig. 4d whose source is undoubtedly due to the coating during FESEM samples preparation. Obviously, the agreement between the experimental and theoretical atomic and weight percentages is better for the insets of Fig. 4e, f. The Gold peak that appears in the inset of Fig. 4d deteriorates the analogy between the measured and computed values. Generally, the discrepancy between EDAX experimental and calculated values is linked to several factors. The inevitable statistical deviations accompanied the EDAX histograms. Also, the beam itself may destroy parts of the sample, produce local degradation of conductive coating, and yield carbon deposition. Moreover, EDAX is just a
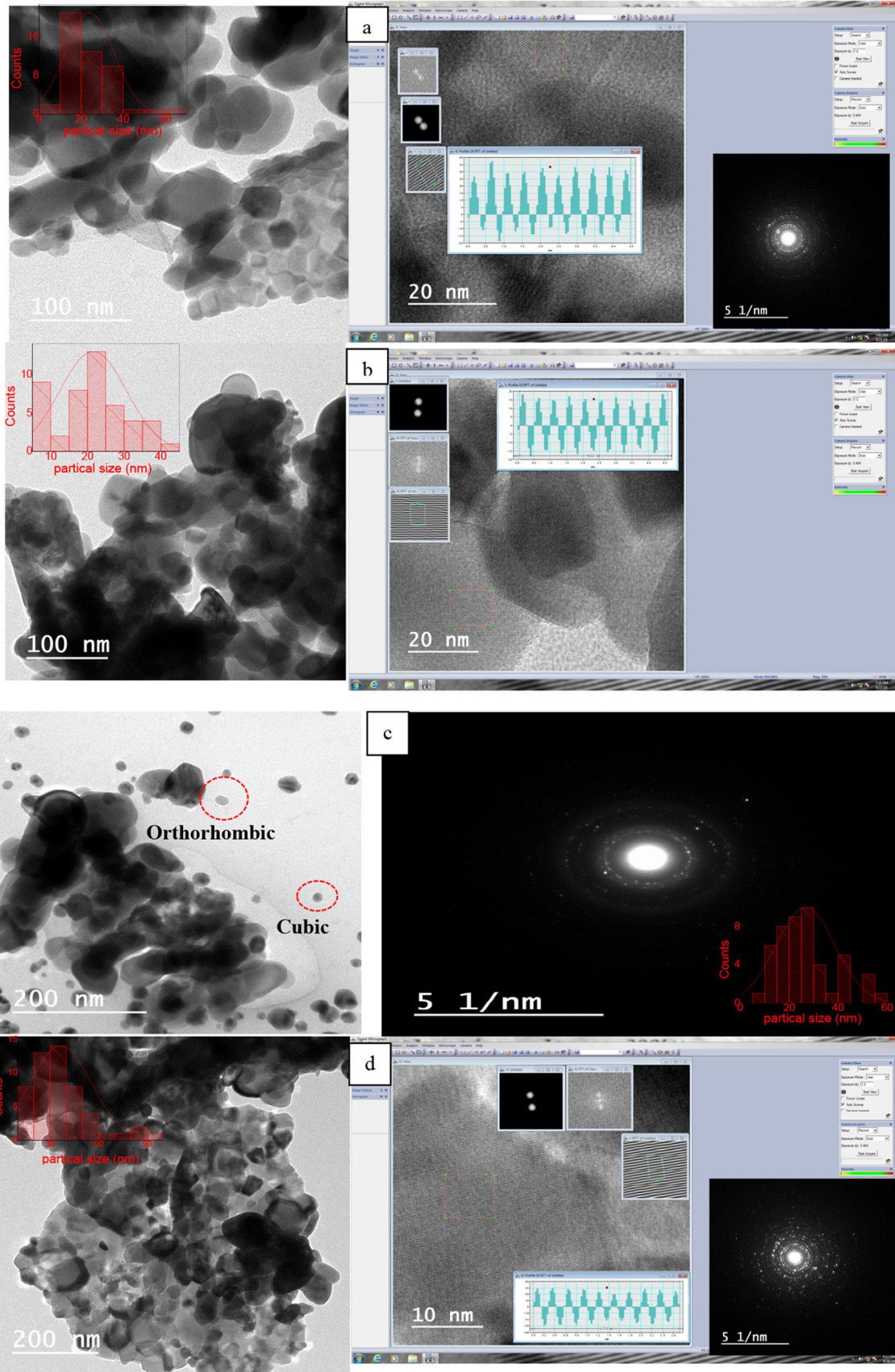
◄**Fig. 3 a–d** HRTEM micrographs with the selected area electron diffraction patterns (SAED) and "d" spacing of the samples [(1-x) CFO + (x) SLFO; x = 0, 0.3, 0.5, and 0.7]
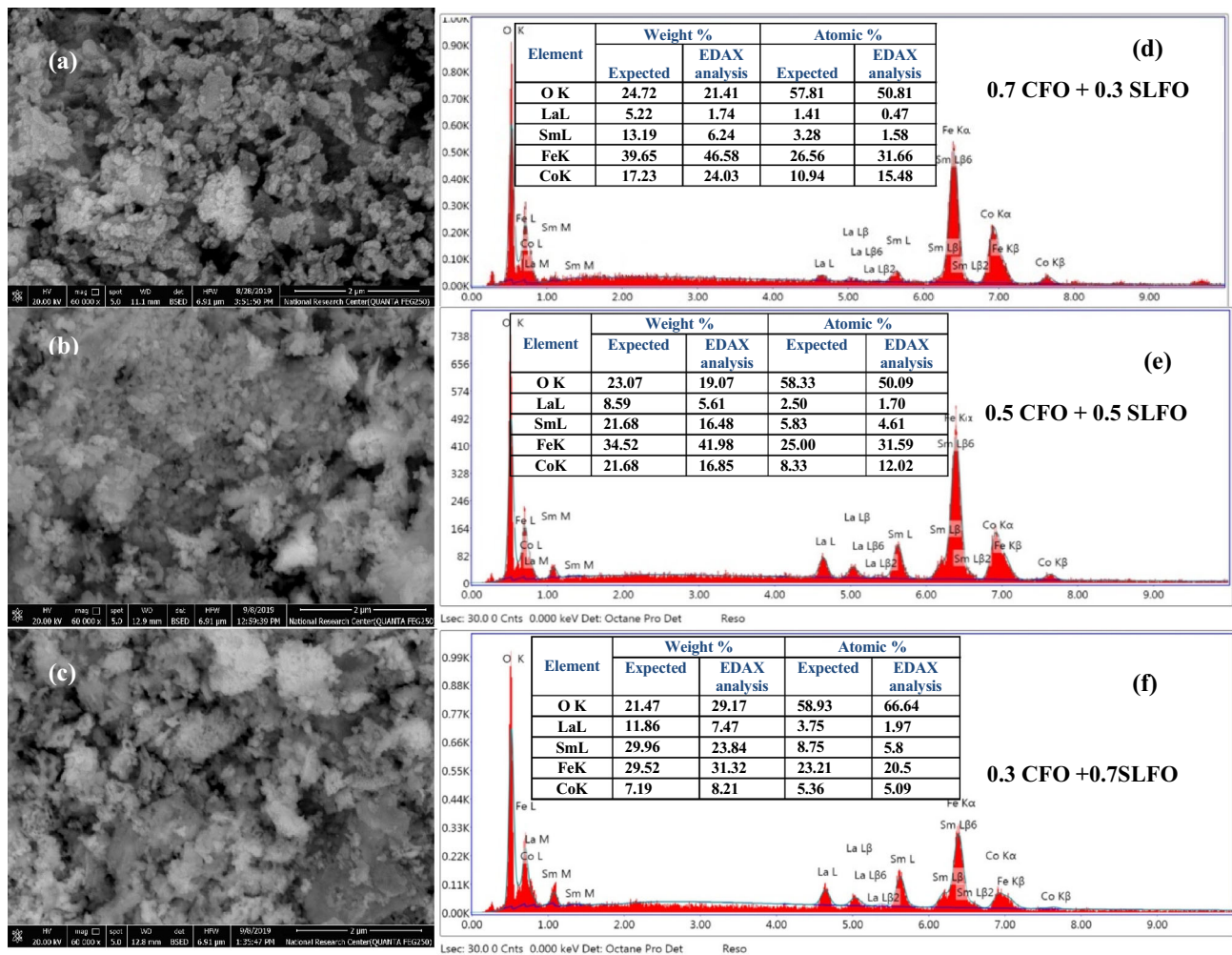
surface sensitive technique, as it only probes the surface down to about 20 μm.

FTIR is used to identify the functional groups of the two parents and the investigated nano-composites. Generally, the most important region in any FTIR spectrum is that in-between 400 and 1500 cm^{-1}. It is called the fingerprint region since it is normally used to pinpoint the different compounds. We will concentrate on the spinel ferrites signature peaks, which exist in the far infrared region. Figure 5 shows the band, $\bar{u}_7$, around 405 cm^{-1} associated with the bending vibration of octahedral metal–oxygen ions.

In addition to, the wider absorption band, $\bar{u}_6$, from 555 to 574 cm^{-1} that corresponds to the stretching vibration of tetrahedral metal–oxygen ions [14]. The bands $\bar{u}_6$ and $\bar{u}_7$ are diverse as a result of the dissimilar octahedral and tetrahedral Fe^{3+}-O^{2-} bond lengths. The higher frequency band, $\bar{u}_6$, has its minimum for SLFO and maximum for CFO and it shifts toward higher frequency as the CFO percentage rises in the nano-composite. The bond force constant is presumed, for the harmonic approximation, as

$$k = 4\pi^2 \bar{v}^2 c^2 \mu \tag{3}$$

where μ is the reduced mass of ions that exist on either side of the bond [15]. Table 2 shows that the force constant of the band $\bar{u}_6$ has a minimum for SLFO and its value increases as the CFO percentage increases. The corresponding vibration frequency

(d) 0.7 CFO + 0.3 SLFO

Element	Weight %		Atomic %	
	Expected	EDAX analysis	Expected	EDAX analysis
O K	24.72	21.41	57.81	50.81
LaL	5.22	1.74	1.41	0.47
SmL	13.19	6.24	3.28	1.58
FeK	39.65	46.58	26.56	31.66
CoK	17.23	24.03	10.94	15.48

(e) 0.5 CFO + 0.5 SLFO

Element	Weight %		Atomic %	
	Expected	EDAX analysis	Expected	EDAX analysis
O K	23.07	19.07	58.33	50.09
LaL	8.59	5.61	2.50	1.70
SmL	21.68	16.48	5.83	4.61
FeK	34.52	41.98	25.00	31.59
CoK	21.68	16.85	8.33	12.02

(f) 0.3 CFO +0.7SLFO

Element	Weight %		Atomic %	
	Expected	EDAX analysis	Expected	EDAX analysis
O K	21.47	29.17	58.93	66.64
LaL	11.86	7.47	3.75	1.97
SmL	29.96	23.84	8.75	5.8
FeK	29.52	31.32	23.21	20.5
CoK	7.19	8.21	5.36	5.09

Fig. 4 a–f Analysis of the synthesized nano-composites; **a–c** FESEM micrographs, **d–f** EDAX elemental analysis and theoretical estimation for atomic (At %) and weight (Wt %) percentages of individual elements
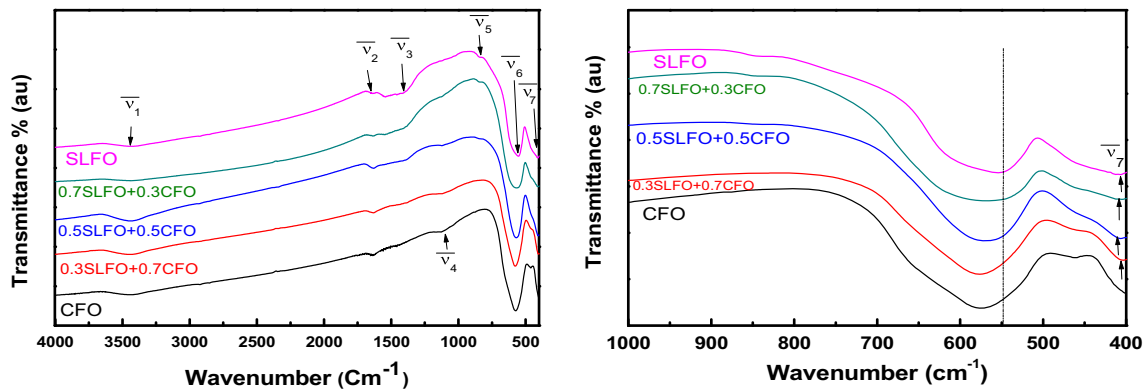
Fig. 5 The FTIR of (1-x) CFO + x SLFO; x = 0, 0.3, 0.5, 0.7, 1 samples

Table 2 Nano-composite signature peaks and corresponding bond force constants for the inspected samples

Sample	$\bar{v}_{66}$ (cm^{-1})	Force constant $K_{\bar{v}_6}$ (dyne/cm) $\times 10^5$	$\bar{v}_7$ (cm^{-1})	Force constant $K_{\bar{v}_7}$ (dyne/cm) $\times 10^5$
CFO	574	2.42	–	–
0.7 CFO + 0.3 SLFO	576	2.44	403	1.19
0.5 CFO + 0.5 SLFO	568	2.37	406	1.21
0.3 CFO + 0.7 SLFO	566	2.35	405	1.20
SLFO	555	2.26	407	1.22

depends on the reduced mass, bond length [16], as well as ions interactions [17], whereas the band intensity is related to the change of the dipole moment with atoms displacement and to its anharmonicity extent [18]. This may explain why the intensity of the nano-composite (0.5 SLFO + 0.5 CFO), graph is not shown, is slightly higher than that of the other samples. Thereafter, the other bands in the spectrum are designated separately. The bands around 3444 cm^{-1} and 1635 cm^{-1} are corresponding to OH stretching vibration of weakly bound water molecules and OH bending vibration mode, respectively [19], while the band 1650–1630 cm^{-1} indicates the presence of C = O double bond [20]. The bands from 1118 to 1130 cm^{-1} indicate the presence of carbonate group, while the bands around 840 and 1400 cm^{-1} designate C-H out-of-plane and in-plane bend [15]. The existence of OH and CO functional groups in the spectra is anticipated simply due to in-air sample measurements.

The magnetic properties of all prepared samples are studied using the vibrating sample magnetometer (VSM). The inset of Fig. 6 is the hysteresis loop for $Sm_{0.7}La_{0.3}FeO_3$ sample which displays antiferromagnetic type. However, the small values of Mr, Hc, lack of the saturation, wide width, and small values of
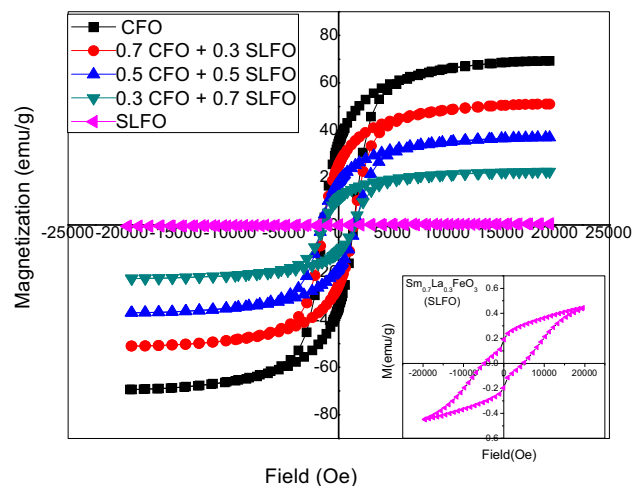
Fig. 6 The M-H hysteresis loops for (1-x) CFO + (x) SLFO; x = 0.0, 0.3, 0.5, 0.7, 1

magnetization designate the non-collinear antiferromagnetic behavior of $Sm_{0.7}La_{0.3}FeO_3$ samples [21]. The magnetic properties of this sample is originated from the possible super exchange (SE) interaction combinations in-between Fe^{3+} and RE^{3+} ions via O^{2-} anion. The dominant SE interaction is the isotropic Fe^{3+}-O-Fe^{3+} which is responsible for the antiparallel alignment of Fe spins leading to anti-ferromagnetism

(AFM) [13]. The Fe^{3+} spins are not completely antiparallel to each other, rather a small angle exists between them (Dzyaloshinsky–Moriya antisymmetric exchange mechanism) which leads to the weak ferromagnetic behavior of the sample [22].

All hysteresis loops display ferrimagnetic hysteresis shape, as would be expected for CFO, except for SLFO sample which displays antiferromagnetic behavior as explained above.

The magnetic parameters as coercivity (H_c), saturation magnetization (M_s), and remnant magnetization (M_r) are tabulated in Table 3. Evidently, both M_s and M_r decrease as SLFO content increases. Moreover, the magnetic parameters M_s and H_c are dependent on several factors, for example, the material microstructure including crystal shape and size [23]. Besides, the area of the hysteresis loop is a measure of the magnetic energy loss.

From saturation magnetization and molecular weight data, one can calculate the magnetic moment per molecule (μ_{eff}) for all the samples according to the following equation[24]

$$\mu_{eff} = \frac{M_s \times M_w}{5585} \tag{4}$$

where M_s is the saturation magnetization and M_w is the molecular weight. μ_{eff} gives the number of Bohr Magnetons (BM) per molecule. The data indicate that the magnetic moment of the nano-composites is enhanced by adding CFO. This is specifically due to the increase in saturation magnetization with the growth of CFO percentage in the composite.

From the magnetic data, detailed in Table 3, the observed squareness ratio (M_r/M_s) is 0.5 for CFO and deviates only slightly from this value for the nano-composites. Nevertheless, the divergence is considerable for SLFO. However, for an assembly of non-interacting particles, according to the Stoner–Wohlfarth (SW) model, the squareness ratio is 0.5 for

uniaxial anisotropy and 0.832 for cubic anisotropy [21]. Therefore, the obtained data confirm the multi-domain particles assembly for the prepared samples [25].

Crystalline, shape, stress, and even surface anisotropies are often related with anomalous magnetic properties [26]. As can be seen from FESEM micrographs, the nano-composites show elongated particles with different sizes which mean that shape anisotropy is crucial for these composites. Additionally, the HRTEM grain and XRD crystallite sizes are different, as discussed above, partially because of the crystals stress.

In the bulk magnetic materials and multi-domain particles, the magnetization is controlled by domain wall movement. However, for single-domain magnetic NPs, the magnetization reversal is only correlated to its magnetic anisotropy. For the case of uniaxial anisotropy, with a first-order anisotropy constant K_1, volume of nanoparticle V, and angle θ between the magnetization direction and the easy axis of magnetization, the uniaxial anisotropy energy, E_{UA}, is given, to first order, as

$$E_{UA} = K_0 + K_1 V \sin^2\theta \tag{5}$$

The anisotropy constant, K_1, may, therefore, be called the anisotropy energy per unit volume [27]. In cubic crystals, the magnetic interaction of electron spin and its orbital angular momentum is the main source of the cubic anisotropy energy. The cubic anisotropy energy density, to first order, takes the form,

$$E_C = K_0 + K_1(m_x^2 m_y^2 + m_y^2 m_z^2 + m_x^2 m_z^2) \tag{6}$$

where m_x, m_y, and m_z are the Cartesian components of the magnetization unit vector, defined as

$$\vec{m} = \vec{M}/M_S \tag{7}$$

Table 3 Coercivity (H_c), saturation magnetization (M_s), remnant magnetization (M_r), squareness (M_s/M_r), magnetic moment (μ_{eff}), energy loss, and ($H_c.M_s$) product

Sample	H_c (Oe)	M_s (emu/g)	M_r (emu/g)	M_r/M_s	μ_{eff} (BM)	Energy loss(erg/g) $\times 10^5$	$H_c.M_s$ (erg/cm^3) $\times 10^6$
CFO	1391.7	69.273	34.716	0.501	2.91	2.80	6.39
0.7 CFO + 0.3 SLFO	1389.1	51.054	25.3	0.496	2.19	2.11	5.33
0.5 CFO + 0.5 SLFO	1544.7	36.994	18.3	0.493	1.61	1.67	4.45
0.3 CFO + 0.7 SLFO	1394.7	22.544	11.2	0.496	0.99	0.974	2.55
SLFO	4848.8	0.44725	0.191	0.427	0.02	0.069	0.193

with $\vec{M}$ is the magnetization and M_S is the saturation magnetization. For $K_1 > 0$, there are six equivalent energy minima corresponding to the positive and negative x, y and z directions [28].

The magneto-crystalline anisotropy energy of cubic $CoFe_2O_4$ is somewhat large with a positive anisotropy constant. The crystal cube edges, $< 1\ 0\ 0 >$, defines the six easy magnetization directions while the four hard directions are along the body diagonals, $< 1\ 1\ 1 >$ [29]. In general, the anisotropic constant value depends on the particle size, lattice parameters, bond lengths, and angles as well as several other structure parameters [30].

According to SW model, the magneto-crystalline anisotropy constant (K_1) of NPs, with cubic anisotropy, is given in terms of H_c and M_s as [31]:

$$H_c = \frac{2K_1}{\mu_0 M_s} \qquad (8)$$

where μ_0 is the universal constant of permeability in free space.

The calculated cubic anisotropy constant of CFO is 3.19×10^6 erg/cm^3 which is comparable to the previously published data of 2.23×10^6 erg/cm^3 with particle size of 8.5 nm [27]. In this work, the average size of the prepared CFO particles is 21.3 nm as obtained from HRTEM micrograph.

Alternatively, we calculate the cubic anisotropy constant of $CoFe_2O_4$, by applying the Law of Approach to saturation [32]. For applied fields (H) much higher than the coercivity, the magnetization (M) is given as:

$$M = M_s\left(1 - \frac{b}{H^2}\right) + \kappa H \qquad (9)$$

where $b = 8K_1^2/(105\mu_0^2 M_s^2)$, M_s is the saturation magnetization, μ_0 is the permeability of the free space, K_1 is the cubic anisotropy constant, and the term κH is the forced magnetization and will be neglected in this approximation. A minimization of the sum of squared residuals (SSR) is carried out for high applied fields, $H > 1$ T, by varying the parameters b and M_s hence the optimum anisotropy constant is calculated. A value of 1.75×10^6 erg/cm^3 is found for the cubic anisotropy constant of CFO. Figure 7 shows the experimental and fitted magnetizations as obtained from the Law of Approach. Otherwise, the law of Approach to saturation may also be utilized to find the susceptibility, at high applied fields, by direct differentiation of equation [2]

$$\chi = \frac{\partial M}{\partial H} \cong \frac{\alpha K_1^2}{M_s H^3} \qquad (10)$$

where $\alpha = 0.152$ for cubic anisotropy. Performing a best linear fit between χ and $1/H^3$, for high fields, $H > 1$ T. Figure 8 shows the best fit line with zero intercept. The cubic anisotropy constant of CFO is found from the slope as $K_1 = 2.39 \times 10^6$ erg/cm^3. The computed values for CFO anisotropy constant are presented in Table 4.

If the hysteresis loop measurement had been done along certain crystallographic direction, then the energy loss per cycle, as given by the loop area, equals the anisotropy energy stored in the crystal magnetized in this particular direction [33]. However, for measurements on poly-crystalline materials, as in this work, a proportionality is anticipated. This is fulfilled by the obvious monotonous relation of the last two columns of Table 3, representing the energy loss and the "$H_c.M_s$" product. From the calculated data, Table 3, we notice that the product "$H_c.M_s$," which is proportional to the magneto-crystalline anisotropy constant, decreases by increasing the SLFO content due to the relatively much higher drop in saturation magnetization than the relative rise of the coercivity.

Notably, various NPs measurements from different researches change sometimes considerably. Variations in preparation techniques, sintering temperature, purity of used materials, and order of preparation steps are just some explanations for the discrepancy of NPs quantities. For instance, the critical size that defines the transition from single-domain to multi-domain NPs for CFO has been
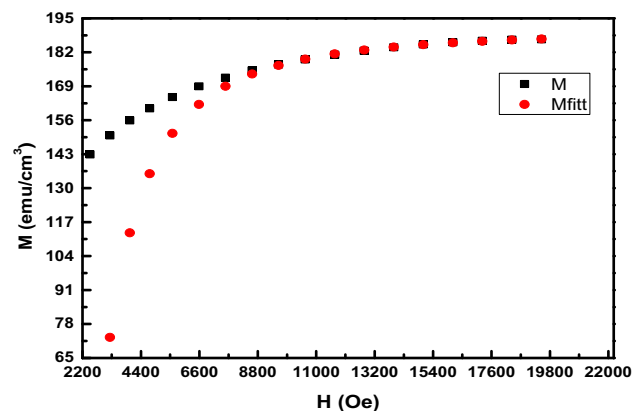
Fig. 7 The fitted and experimental magnetizations as a function of the applied field
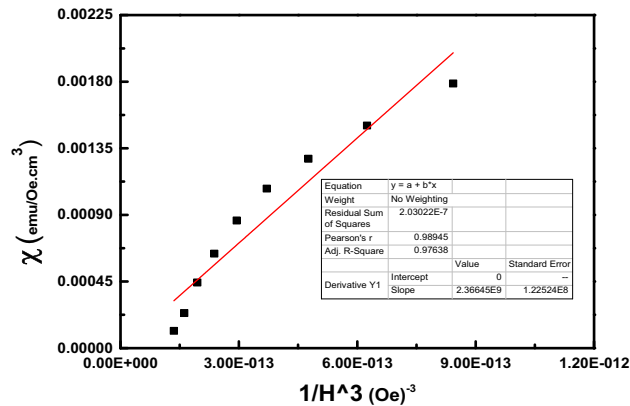
Fig. 8 Linear best fit analysis of susceptibility versus reciprocal of (applied field)^3

disputed in literature; significantly different values of 50 nm[34], 40 nm [35], and 28 nm[36], as well as several other different values have already been reported. In this study, the critical size, D_C, is estimated by applying the formula [37], in cgs system of units,

$$D_C = \frac{9\gamma}{2\pi M_S^2} \tag{11}$$

where Ms is the saturation magnetization in Gauss and γ is the domain wall energy per unit area and is given as follows:

$$\gamma = \left[\frac{2K_B T_C |K_1|}{a}\right]^{\frac{1}{2}} \tag{12}$$

where T_C is the Curie temperature, K_B is the Boltzmann constant, a is the lattice constant, and K_1 is the anisotropy constant. Substituting for T_C = 833 K [38], K_1 is taken as the average of the three values calculated in this study which is 2.44×10^6 erg/cm^3 and "a" is the lattice constant of CFO as given in Table 1. The domain wall energy density is found to be 2.59 erg/cm^3 and the critical size value is 1.76 nm. Apparently, the stated critical size is rather quite small relative to the formerly published data. Two

main reasons for this inconsistency. The critical size is a very sensitive function of the particle dimension. More importantly, the shape, stress, and surface anisotropies need to be included in the calculations. Presumably, these diverse anisotropies will lead to an effective anisotropy constant, K_{eff}, given as the sum of the individual constants.

$$K_{eff} = K_1 + K_{sh} + K_s + K_{st} \tag{13}$$

where K_{sh}, K_s, and K_{st} are the shape, surface, and stress anisotropy constants, respectively [39].

Since the crystallite size is one of the crucial factors that enhances the coercivity. Therefore, the relatively large coercivity for the nano-composite, x = 0.5, as indicated from Table 3, could be explained by its relatively large individual crystal sizes of CFO and SLFO, as shown from Table 1. Also, the high saturation magnetization of CFO, knowing that the bulk value is 80.8 emu/g [40], is consistent with its relatively large crystallite size. Since, close to single-domain region, as the crystallite size increases, the magnetic domain size will subsequently grow, hence the number of atomic spins in the domain increases, which leads to augmentation of the saturation magnetization.

As the nano-composites are formed by mere physically mixing CFO and SLFO, we expect the magnetic measurements for the nano-composites and those of the two parents to be related because of the short-range interaction of magnetic entities. Let Q refers to either quantity of M_s, M_r, or μ_{eff} for the nano-composite, whereas Q_1 and Q_2 are the corresponding quantities of the two parents CFO and SLFO, respectively. Within the validity of negligible interaction assumption, the value of the measured quantity for the nano-composite (Q) is expected to be the weighted sum of the corresponding quantities of the two parents (Q_1, Q_2). Indeed, we test this assumption to compute the above-mentioned magnetic parameters for the nano-composites by applying the proposed formula,

Table 4 A summary of the calculated values of the anisotropic constant for CFO along with their method of evaluation

| Physical property	Value $\times 10^6$ (erg/cm^3)	Calculation method		Reference
CFO cubic anisotropy constant	3.19	Equation (8)	Direct substitution	This study
	1.75	Equation (9)	Curve Fitting	
	2.37	Equation (10)	Linear best fit	
	2.23	Direct substitution		[27]

Table 5 The experimental, calculated, and percentage errors of M_s, M_r, and μ_{eff} for the different nano-composites

Sample	M_s (emu/g)			M_r (emu/g)			μ_{eff} (BM)		
	Experimental	Calculated	% Error	Experimental	Calculated	% Error	Experimental	Calculated	% Error
CFO	69.273	–	–	34.716	–	–	2.91	–	–
0.7 CFO + 0.3 SLFO	51.054	48.625	4.8	25.3	24.359	3.7	2.19	2.04	6.7
0.5 CFO + 0.5 SLFO	36.994	34.860	5.8	18.3	17.454	4.6	1.61	1.47	9.0
0.3 CFO + 0.7 SLFO	22.544	21.095	6.4	11.2	10.549	5.8	0.99	0.89	10.4
SLFO	0.44725	–	–	0.191	–	–	0.02	–	–

$$Q = (1 - X) \times Q_1 + X \times Q_2 \qquad (14)$$

Then, the calculated and experimental values are used to find the percentage errors, Table 5, which turned out to be less than 6.5, 6, and 10.5 for M_s, M_r, and μ_{eff}, respectively. These errors could be explained partially by the powder losses in the mortar walls during the mixing process; therefore, the mixing parameter, X, is expected to change as a result of the mixing. Also, the individual crystallite sizes of CFO and SLFO are varying due to the mixing, as indicated from Table 1, which consequently leads to a change of the individual magnetic parameters. Moreover, in accordance with the short-range magnetic interaction, some amounts, rather tiny, of magnetic entities are influencing each other during the physical mixing.

Furthermore, the statistical and stochastic deviations of the physical quantities assessment have their unambiguous role in measurements fluctuations. On the other hand, H_c values for the nano-composites clearly do not follow this simple formula. The coercivity is highly dependent on several factors, for example, the surface roughness, grain size, and residual stain [41]. Moreover, Hc varies a lot around the critical size, as shown in the schematic Fig. 9. Either in the single-domain or in the multi-domain regions, the coercivity drops rapidly as the nanoparticle size deviates from the critical size. In the multi-domain region, the escalation of Hc with the drop of grain size, D, is proportional to $1/D$, since the formation of a closed magnetic flux, in small particles, turns out to be energetically less favorable. Therefore, the magnetic domain size, with a uniform magnetization, coincides more and more with the
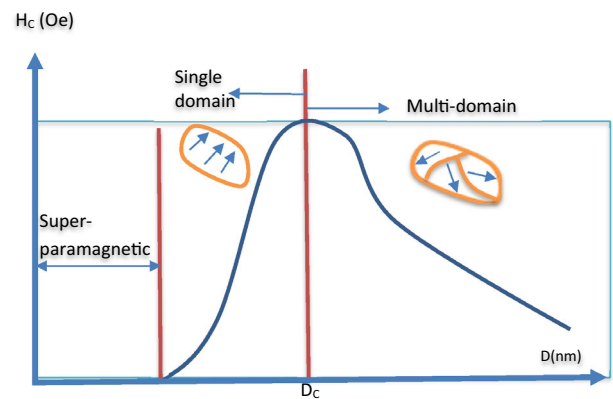
Fig. 9 Schematic diagram showing the variation of the coercivity with the particle size around the critical size (D_C)

grain size itself. Hence, as the change of magnetization in this case cannot occur by shifting the domain walls, which normally requires weaker magnetic fields, the coercivity or remanence will show a sharp rise as the critical size is approached [35].

4 Conclusion

The nano-composites and the parents are prepared without secondary phases detected. The squareness ratio for CFO is 0.5 and that of the nano-composites varies slightly from this value. For cubic anisotropy, as is the case for CFO, this indicates that the particles are in the multi-phase regime. The magneto-crystalline anisotropy constant is calculated from three different approaches and the obtained values are in the range of 1.75–3.19 × 10^6 erg/cm^3 for average particle size of 21 nm, which is in remarkable

agreement with prior issued reports. A rough estimation of CFO critical size leads to a value of 1.76 nm which is rather smaller than the disputed range of values in literature. Inclusion of shape, surface, and stress anisotropies will definitely enhance the critical size assessment, a proposition which will be dealt with in a future plan. We examine a suggestion for evaluating the M_s, M_r, and μ_r values for the physically mixed nano-composites by the weighted sum of the corresponding quantities of the two parents. We found a good agreement between the evaluated and experimental values.

References

1. Y.H. Hou et al., Structural, electronic and magnetic properties of partially inverse spinel $CoFe_2O_4$: a first-principles study. J. Phys. D. Appl. Phys. (2010). https://doi.org/10.1088/0022-3727/43/44/445003

2. S. Jauhar, J. Kaur, A. Goyal, S. Singhal, Tuning the properties of cobalt ferrite: a road towards diverse applications. RSC Adv. **6**(100), 97694–97719 (2016). https://doi.org/10.1039/c6ra21224g

3. T. Yu, Z.X. Shen, Y. Shi, J. Ding, Cation migration and magnetic ordering in spinel $CoFe_2O_4$ powder: Micro-Raman scattering study. J. Phys. Condens. Matter. (2002). https://doi.org/10.1088/0953-8984/14/37/101

4. L.J. Berchmans, V. Leena, K. Amalajyothi, S. Angappan, A. Visuvasam, Preparation of lanthanum ferrite substituted with MG and CA. Mater. Manuf. Process. **24**(5), 546–549 (2009). https://doi.org/10.1080/10426910902746739

5. L. Wu et al., Monolayer assembly of ferrimagnetic $Co_xFe_{3-x}O_4$ nanocubes for magnetic recording. Nano Lett. **14**(6), 3395–3399 (2014). https://doi.org/10.1021/nl500904a

6. J.A. Paulsen, A.P. Ring, C.C.H. Lo, J.E. Snyder, D.C. Jiles, Manganese-substituted cobalt ferrite magnetostrictive materials for magnetic stress sensor applications. J Phys Appl (2005). https://doi.org/10.1063/1.1839633

7. A.B. Stambouli, E. Traversa, Solid oxide fuel cells (SOFCs): A review of an environmentally clean and efficient source of energy. Renew. Sustain. Energy Rev. **6**(5), 433–455 (2002). https://doi.org/10.1016/S1364-0321(02)00014-X

8. Y.M. Zhang, Y.T. Lin, J.L. Chen, J. Zhang, Z.Q. Zhu, Q.J. Liu, A high sensitivity gas sensor for formaldehyde based on silver doped lanthanum ferrite. Sensors Actuators, B Chem. **190**, 171–176 (2014). https://doi.org/10.1016/j.snb.2013.08.046

9. F. Tang Li, Y. Liu, R. Hong Liu, Z. Min Sun, D. Shun Zhao, C. Guang Kou, Preparation of Ca-doped LaFeO3 nanopowders in a reverse microemulsion and their visible light photocatalytic activity". Mater. Lett. **64**(2), 223–225 (2010). https://doi.org/10.1016/j.matlet.2009.10.048

10. N. Sanpo, C.C. Berndt, C. Wen, J. Wang, Transition metal-substituted cobalt ferrite nanoparticles for biomedical applications. Acta Biomater. **9**(3), 5830–5837 (2013). https://doi.org/10.1016/j.actbio.2012.10.037

11. M. I. A. A. Maksoud et al., Antibacterial, antibiofilm, and photocatalytic activities of metals-substituted spinel cobalt ferrite nanoparticles. Elsevier Ltd. **127** (2019)

12. M.A. Ahmed, N.G. Imam, M.K. Abdelmaksoud, Y.A. Saeid, Magnetic transitions and butterfly-shaped hysteresis of Sm-Fe-Al-based perovskite-type orthoferrite. J. Rare Earths **33**(9), 965–971 (2015). https://doi.org/10.1016/S1002-0721(14)60513-5

13. E.E. Ateia, H. Ismail, H. Elshimi, M.K. Abdelmaksoud, Structural and magnetic tuning of LaFeO3 orthoferrite substituted different rare earth elements to optimize their technological applications, under puplication. J. Inorgan. Organometall. Polym. Mater. (2020). https://doi.org/10.1088/2053-1591/abd73b

14. K.S. Rao, G.S.V.R.K. Choudary, K.H. Rao, C. Sujatha, Structural and magnetic properties of ultrafine $CoFe_2O_4$ nanoparticles. Procedia Mater. Sci. **10**, 19–27 (2014). https://doi.org/10.1016/j.mspro.2015.06.019

15. J. Coates, Encyclopedia of Analytical Chemistry -IInterpretation of Infrared Spectra, A Practical Approach. Encycl. Anal. Chem. 1–23, (2004)

16. O.M. Hemeda, M.M. Barakat, D.M. Hemeda, Structural, electrical and spectral studies on double rare-earth orthoferrites $La_{1-x}Nd_xFeO_3$. Turkish J. Phys. **27**(6), 537–549 (2003). https://doi.org/10.3906/sag-1205-29

17. B.C. Smith, *Fundamentals of Fourier Transform Infrared Spectroscopy*, 2nd edn. (CRC Press, Boca Raton, 2011).

18. C. Pasquini, Near infrared spectroscopy: Fundamentals, practical aspects and analytical applications. J. Braz. Chem. Soc. **14**(2), 198–219 (2003). https://doi.org/10.1590/S0103-50532003000200006

19. N. Adhlakha, K.L. Yadav, R. Singh, BiFeO3–CoFe2O4–PbTiO3 composites: structural, multiferroic, and optical characteristics. J. Mater. Sci. **50**(5), 2073–2084 (2015). https://doi.org/10.1007/s10853-014-8769-z

20. C. Berthomieu, E. Nabedryk, W. Mäntele, J. Breton, Characterization by FTIR spectroscopy of the photoreduction of the primary quinone acceptor QA in photosystem II. FEBS Lett. **269**(2), 363–367 (1990). https://doi.org/10.1016/0014-5793(90)81194-S

21. T. Ibusuki, S. Kojima, O. Kitakami, Y. Shimada, Magnetic anisotropy and behaviors of Fe. IEEE Trans. Magn. **37**(4), 2223–2225 (2001)

22. S. Yuvaraj, S. Layek, S.M. Vidyavathy, S. Yuvaraj, D. Meyrick, R.K. Selvan, Electrical and magnetic properties of spherical $SmFeO_3$ synthesized by aspartic acid assisted combustion method. Mater. Res. Bull. **72**, 77–82 (2015). https://doi.org/10.1016/j.materresbull.2015.07.013

23. A. Amirabadizadeh, Z. Salighe, R. Sarhaddi, Z. Lotfollahi, Synthesis of ferrofluids based on cobalt ferrite nanoparticles: Influence of reaction time on structural, morphological and magnetic properties. J. Magn. Magn. Mater. **434**, 78–85 (2017). https://doi.org/10.1016/j.jmmm.2017.03.023

24. M.A. Ahmed, S.F. Mansour, H. Ismael, A comparative study on the magnetic and electrical properties of $MFe_{12}O_{19}$ (M=Ba and Sr)/BiFeO3 nanocomposites. J. Magn. Magn. Mater. **378**, 376–388 (2015). https://doi.org/10.1016/J.JMMM.2014.10.173

25. C. Sudakar, G.N. Subbanna, T.R.N. Kutty, Wet chemical synthesis of multicomponent hexaferrites by gel-to-crystallite conversion and their magnetic properties. J. Magn. Magn. Mater. **263**(3), 253–268 (2003). https://doi.org/10.1016/S0304-8853(02)01572-X

26. L. Horng, G. Chern, M.C. Chen, P.C. Kang, D.S. Lee, Magnetic anisotropic properties in Fe_3O_4 and $CoFe_2O_4$ ferrite epitaxy thin films. J. Magn. Magn. Mater. **270**(3), 389–396 (2004). https://doi.org/10.1016/j.jmmm.2003.09.005

27. A.J. Rondinone, A.C.S. Samia, Z.J. Zhang, Characterizing the magnetic anisotropy constant of spinel cobalt ferrite nanoparticles. Appl. Phys. Lett. **76**(24), 3624–3626 (2000). https://doi.org/10.1063/1.126727

28. M. D'Aquino, Nonlinear magnetization dynamics in thin-films and nanoparticles. Dr. Thesis Electr. Eng. 155, (2004)

29. T. Hyeon, Chemical synthesis of magnetic nanoparticles. 927–934, (2003)

30. A. Lehlooh, S.H. Mahmood, J.M. Williams, On the particle size dependence of the magnetic anisotropy energy constant. Phys B: Condens Mater **321**, 159–162 (2002)

31. Q. Song, Z.J. Zhang, Shape control and associated magnetic properties of spinel cobalt ferrite nanocrystals. J. Am. Chem. Soc. **126**(19), 6164–6168 (2004). https://doi.org/10.1021/ja049931r

32. L. Kumar, M. Kar, Journal of Magnetism and Magnetic Materials Influence of Al^{3+} ion concentration on the crystal structure and magnetic anisotropy of nanocrystalline spinel cobalt ferrite. J. Magn. Magn. Mater. **323**(15), 2042–2048 (2011). https://doi.org/10.1016/j.jmmm.2011.03.010

33. C. D. G. B D Cullity, Introduction to magnetic materials. 2008.

34. C.N. Chinnasamy et al., Unusually high coercivity and critical single-domain size of nearly monodispersed $CoFe_2O_4$ nanoparticles. Appl. Phys. Lett. **83**(14), 2862–2864 (2003). https://doi.org/10.1063/1.1616655

35. D.S. Mathew, R.S. Juang, An overview of the structure and magnetism of spinel ferrite nanoparticles and their synthesis in microemulsions. Chem. Eng. J. **129**(1–3), 51–65 (2007). https://doi.org/10.1016/j.cej.2006.11.001

36. K. Maaz, A. Mumtaz, S.K. Hasanain, A. Ceylan, Synthesis and magnetic properties of cobalt ferrite ($CoFe_2O_4$) nanoparticles prepared by wet chemical route. J. Magn. Magn. Mater. **308**(2), 289–295 (2007). https://doi.org/10.1016/j.jmmm.2006.06.003

37. C. Sujatha, K. Venugopal Reddy, K. Sowri Babu, A. Ramachandra Reddy, K.H. Rao, Effect of sintering temperature on electromagnetic properties of NiCuZn ferrite. Ceram. Int. **39**(3), 3077–3086 (2013). https://doi.org/10.1016/j.ceramint.2012.09.087

38. E.E. Ateia, M.K. Abdelamksoud, M.A. Rizk, Improvement of the physical properties of novel (1–x) CoFe2O4 + (x) LaFeO3 nanocomposites for technological applications. J. Mater. Sci. Mater. Electron. **28**(21), 16547–16553 (2017). https://doi.org/10.1007/s10854-017-7567-1

39. C. Caizer, M. Stefanescu, Nanocrystallite size effect on σ_s and H_c in nanoparticle assemblies. Phys. B Condens. Matter **327**(1), 129–134 (2003). https://doi.org/10.1016/S0921-4526(02)01785-4

40. L.D. Tung, V. Kolesnichenko, D. Caruntu, N.H. Chou, C.J. O'Connor, L. Spinu, Magnetic properties of ultrafine cobalt ferrite particles. J. Appl. Phys. **93**(102), 7486–7488 (2003). https://doi.org/10.1063/1.1540145

41. Y.C. Wang, J. Ding, J.B. Yi, B.H. Liu, T. Yu, Z.X. Shen, High-coercivity Co-ferrite thin films on (100)-SiO_2 substrate. Appl. Phys. Lett. **84**(14), 2596–2598 (2004). https://doi.org/10.1063/1.1695438